Pure magnon valley currents in a patterned ferromagnetic thin film

Shasha Ke,[1,2] Yun-Mei Li,[3,*] Wen-Kai Lou,[1,2,†] and Kai Chang[1,2,‡]

[1]*SKLSM, Institute of Semiconductors, Chinese Academy of Sciences, Beijing 100083, China*

[2]*College of Materials Science and Opto-electronic Technology, Center of Materials Science and Optoelectronics Engineering, University of Chinese Academy of Sciences, Beijing 100049, China*

[3]*Department of Physics, School of Physical Science and Technology, Xiamen University, Xiamen 361005, China*

(Received 10 April 2022; revised 12 March 2023; accepted 16 March 2023; published 28 March 2023)

We propose a new method to generate pure magnon valley currents in ferromagnetic thin films with triangular antidot lattices. We find that inhomogeneous distortions can generate pseudomagnetic fields which can be up to 60 T for magnons, and give rise to well-defined Landau levels. The pseudomagnetic fields push magnons at different valleys K and K′ transversely to opposite directions and accumulate at opposite edges, leading to magnon valley Hall effect and forming pure magnon valley edge currents. We also find that the oppositely directed pseudomagnetic fields result in magnon snake states at the center of the ribbon, forming pure magnon valley currents. Our work might pave a new way to manipulate magnon transport by using artificial designed structures.

DOI: 10.1103/PhysRevB.107.104426

I. INTRODUCTION

Recently, there is rapidly growing interest to use quasiparticles instead of electrons as potential information carriers, aiming at reducing energy dissipation when the size of quantum devices is shrunk to the nanoscale. One of the most promising candidates is spin-wave spintronics, the so-called magnonics, a field that refers to information communicating and processing through spin waves (collective excitations of the magnetization) [1–4]. In contrast to the traditional magnetic metals or semiconductors, the magnetic insulators, such as yttrium iron garnet (YIG) [3,5–7], offer us a crucial opportunity to realize totally Joule-heat-free information transport. Due to these desirable advantages, YIG has been a prototype material to investigate the physics of many intriguing spin-wave phenomena, such as spin-wave logic, coherent elastic excitation of spin waves, Goos-Hänchen shift of spin-wave beam, spin-wave fiber, and magnetic tweezer [8–12].

Dirac magnons [13–15], a magnetic counterpart of Dirac electrons, have been realized in a patterned ferromagnetic insulator YIG [16]. Artificial antidot lattices can be realized experimentally by etching periodic arrays of holes in a ferromagnetic thin film [17,18]. In artificial lattices, one can engineer the energy spectrum of carriers, e.g., electrons, photons, and magnons, by etching various holes and/or antidots with chiral geometric structures, leading to many interesting features, such as Dirac electrons, photons, or magnons, artifical gauge fields, and topological states [16,19–24]. Since typical magnon energy ranges from gigahertz (GHz) to terahertz (THz) frequency, i.e., the wavelength of magnons is about 100 nm [25–28], therefore it is possible to fabricate artificial antidot lattices with the state-of-the-art techniques. The artificial antidot lattices offer us a novel platform to observe interesting phenomena of magnon spintronics.

In this work, we investigate theoretically the pure magnon valley currents in a ferromagnetic thin film (FTF) with triangular antidot lattices. Using the Landau-Lifshitz-Gilbert (LLG) equation and lattice model, we show that magnons in this system behave as Dirac magnons with a linear dispersion. We also find that the magnon spectra in FTFs with triangular antidot lattices with inhomogeneous distortions show the well-defined Landau level fans, which are caused by the artificial gauge field, i.e., the pseudomagnetic field, generated by the lattice distortions. The pseudomagnetic fields emerging at the K and K′ valleys of the Bullioun zone of the antidot lattices point to opposite directions, and push magnons at the K and K′ valleys to opposite directions, leading to magnon valley Hall effect and forming pure magnon valley edge currents. By designing a specific configuration which generates opposite pseudomagnetic fields in a FTF, we also find that magnon snake states localize at the center of the ribbon due to oppositely directed pseudomagnetic fields $\pm\mathbf{B}$ on the two sides of the ribbon, forming pure magnon valley currents, counterpropagating in snake orbits.

This paper is organized as follows. In Sec. II, the magnon spectra of triangular antidot lattices are calculated based on the LLG equation and tight-binding model, respectively. In Sec. III, we present numerical results and discussions about the pure magnon valley currents in armchair- and zigzag-edged ribbons. Finally, the results of this paper are briefly summarized in Sec. IV.

II. THEORY

As shown in Fig. 1(a), we first consider a two-dimensional (2D) artificial lattice consisting of periodic arrays of holes etched in a FTF, such as YIG. Recently, the experimental

*yunmeili@xmu.edu.cn
†wklou@semi.ac.cn
‡kchang@semi.ac.cn

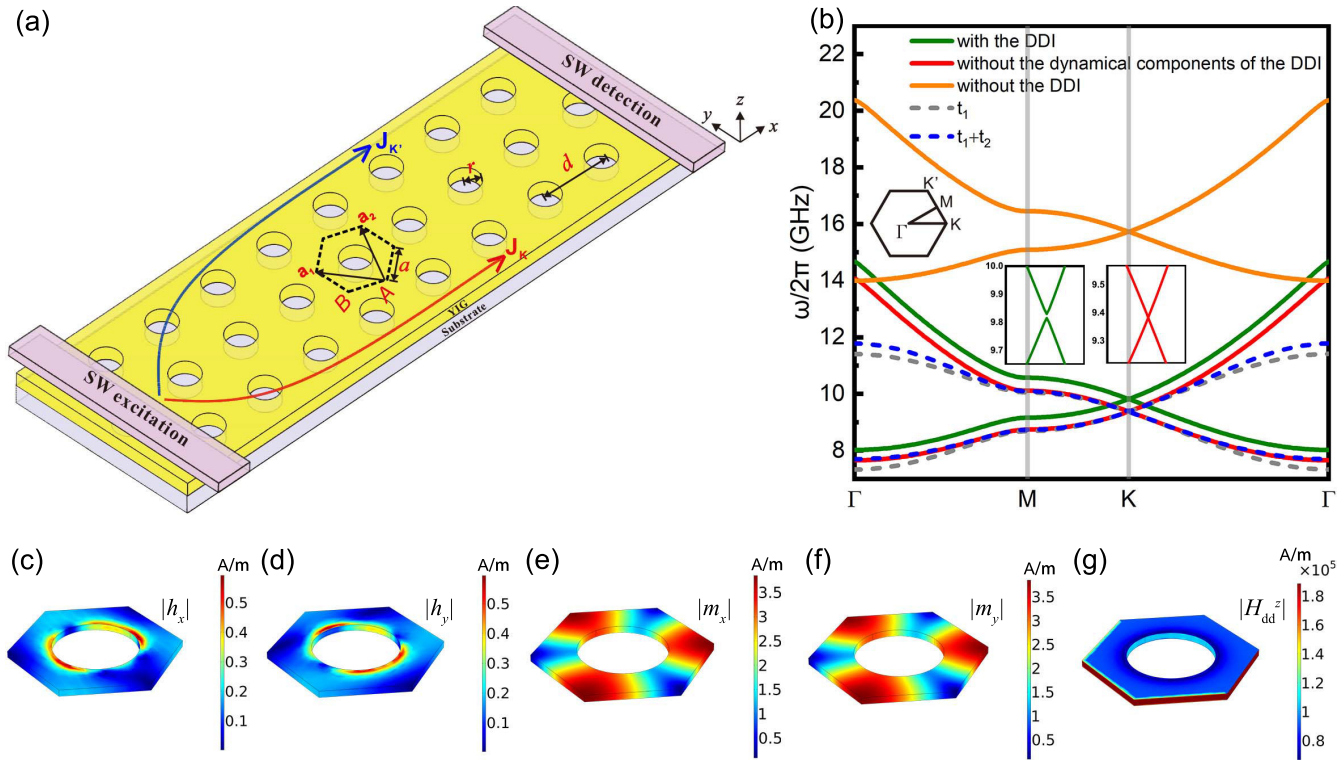

FIG. 1. (a) Schematic of a triangular antidot lattice consisting of circular-shaped holes in a YIG thin film and the pure magnon valley edge currents $\mathbf{J}_{\mathrm{K}}$ and $\mathbf{J}_{\mathrm{K}'}$ arising from K and K′ valleys, respectively. The black dashed hexagon denotes the unit cell of the antidot lattices. The two inequivalent sites in a unit cell are denoted as A and B and the two primitive vectors are denoted as $\mathbf{a_1}$ and $\mathbf{a_2}$. The nearest-neighbor distance is a, the distance between two nearest antidots is d and the radius of antidots is r. (b) The lowest two bands of the magnon spectrum of YIG thin film in a triangular antidot lattice. The green, red, and orange solid lines show the magnon band structures obtained from the LLG equation with the DDI, without considering the dynamical components of the DDI and without the DDI, respectively. The gray and blue dashed lines denote the fitting results using the TB model with the nearest- and next-nearest-neighbor interactions, respectively. The inset above shows the first Brillouin zone of the magnonic crystal. Here, $a = 50$ nm, $r = 25$ nm, and the thickness of the YIG film is assumed as 4 nm. The spatial distributions of the (c) $|h_x|$, (d) $|h_y|$, (e) $|m_x|$, (f) $|m_y|$, and (g) $|H^z_{\mathrm{dd}}|$ at the K (K′) point with the DDI.

group reported a successful fabrication of YIG thin film with the thickness 4 nm and the out-of-plane magnetization [29–31]. The embedded antidots are circular-shaped holes which are arranged in a triangular lattice, i.e., a graphene-like honeycomb configuration for magnons. In antidot lattices, there are two inequivalent sites in a unit cell with basis vectors $\mathbf{a_1} = \frac{\sqrt{3}a}{2}(1, \sqrt{3})$ and $\mathbf{a_2} = \frac{\sqrt{3}a}{2}(-1, \sqrt{3})$, where $a = d/\sqrt{3}$ is the nearest-neighbor distance and d is the distance between two nearest antidots. The corresponding reciprocal-lattice basis vectors are $\mathbf{b_1} = \frac{2\pi}{3a}(\sqrt{3}, 1)$ and $\mathbf{b_2} = \frac{2\pi}{3a}(-\sqrt{3}, 1)$.

The spatiotemporal evolution of the magnetization $\mathbf{M}(\mathbf{r}, t)$, the so-called magnetic dynamics, is governed by the LLG equation

$$\frac{\partial \mathbf{M}(\mathbf{r}, t)}{\partial t} = -\gamma \mathbf{M}(\mathbf{r}, t) \times \mathbf{H}_{\mathrm{eff}}(\mathbf{r}, t) + \frac{\alpha}{M_{\mathrm{s}}} \mathbf{M}(\mathbf{r}, t) \times \frac{\partial \mathbf{M}(\mathbf{r}, t)}{\partial t}, \tag{1}$$

where γ is the gyromagnetic ratio, M_{s} the saturation magnetization, α the Gilbert damping constant, and $\mathbf{H}_{\mathrm{eff}}$ the effective magnetic field consisting of three parts $\mathbf{H}_{\mathrm{eff}} = \mathbf{H}_0 + \mathbf{H}_{\mathrm{ex}} + \mathbf{H}_{\mathrm{dd}}$. The first term is the external magnetic field $\mathbf{H}_0 = H_0 \mathbf{e}_z$ applied perpendicularly to the FTF, the second term is the exchange field $\mathbf{H}_{\mathrm{ex}} = (\nabla \cdot \lambda^2_{\mathrm{ex}} \nabla)\mathbf{M}$, with λ_{ex} being the exchange length, and the third term is the demagnetization field due to the nonlocal dipole-dipole interaction (DDI) between the magnetic moments [32]. In the YIG thin film, the damping effect [the second term of Eq. (1)] is quite weak and could be safely neglected in the following calculations in this paper without loss of generality [33]. Moreover, the magnetization $\mathbf{M}(\mathbf{r}, t)$ processes around the direction of the saturation magnetization, which can be divided into the out-of-plane (static) and the in-plane (dynamical) components $\mathbf{M}(\mathbf{r}, t) = M_{\mathrm{s}} \mathbf{e}_z + \mathbf{m}(\mathbf{r}, t)$, with $|\mathbf{m}(\mathbf{r}, t)| \ll M_{\mathrm{s}}$. Meanwhile, the demagnetization field $\mathbf{H}_{\mathrm{dd}}(\mathbf{r}, t)$ can also be correspondingly divided into two components $\mathbf{H}_{\mathrm{dd}}(\mathbf{r}, t) = H^z_{\mathrm{dd}} \mathbf{e}_z + \mathbf{h}(\mathbf{r}, t)$, with $|\mathbf{h}(\mathbf{r}, t)| \ll H^z_{\mathrm{dd}}$. Defining two complex fields $\tilde{m}(\mathbf{r}, t) = m_x(\mathbf{r}, t) - i m_y(\mathbf{r}, t)$ and $\tilde{h}(\mathbf{r}, t) = h_x(\mathbf{r}, t) - i h_y(\mathbf{r}, t)$, we can write the dissipationless LLG equation as

$$i\frac{\partial \tilde{m}(\mathbf{r}, t)}{\partial t} = \gamma \left(H_0 + H^z_{\mathrm{dd}}\right)\tilde{m}(\mathbf{r}, t) - \gamma M_{\mathrm{s}} \lambda^2_{\mathrm{ex}} \nabla^2 \tilde{m}(\mathbf{r}, t) - \gamma M_{\mathrm{s}} \tilde{h}(\mathbf{r}, t). \tag{2}$$

In our calculations, we adopt the exchange boundary condition $\mathbf{n} \cdot \nabla \tilde{m}(\mathbf{r}, t) = 0$ [34], where $\mathbf{n}$ is the normal direction of the boundary. Similar to solving for the Schrödinger

equation in periodic structures, we adopt $\tilde{m}(\mathbf{r},t)=\tilde{m}_{\mathbf{k}}(\mathbf{r})e^{i(\mathbf{k}\cdot\mathbf{r}-\omega t)}$ and $\tilde{h}(\mathbf{r},t)=\tilde{h}_{\mathbf{k}}(\mathbf{r})e^{i(\mathbf{k}\cdot\mathbf{r}-\omega t)}$, where $\mathbf{k}$ is the in-plane wavevector in the first Brillouin zone and ω is the frequency of spin waves. Then Eq. (2) can be reduced to an eigenvalue equation

$$\omega\tilde{m}_{\mathbf{k}}(\mathbf{r})=\gamma\left[H_0+H_{\mathrm{dd}}^z-M_{\mathrm{s}}\lambda_{\mathrm{ex}}^2(-\mathbf{k}^2+2i\mathbf{k}\cdot\nabla+\nabla^2)\right]\tilde{m}_{\mathbf{k}}(\mathbf{r})-\gamma M_{\mathrm{s}}\tilde{h}(\mathbf{r}), \tag{3}$$

and the exchange boundary reads $\mathbf{n}\cdot\nabla\tilde{m}_{\mathbf{k}}(\mathbf{r})+i\mathbf{n}\cdot\mathbf{k}\tilde{m}_{\mathbf{k}}(\mathbf{r})=0$.

The demagnetization field in the FTF fulfills the Maxwell's equations [35]

$$\nabla\times\mathbf{H}_{\mathrm{dd}}(\mathbf{r})=0,\ \nabla\cdot[\mathbf{H}_{\mathrm{dd}}(\mathbf{r})+\mathbf{M}(\mathbf{r})]=0. \tag{4}$$

According to Eq. (4), we introduce the magnetostatic potential $\Psi(\mathbf{r})$, which is satisfied

$$\mathbf{H}_{\mathrm{dd}}(\mathbf{r})=-\nabla\Psi(\mathbf{r})=H_{\mathrm{dd}}^z\mathbf{e}_z+\mathbf{h}(\mathbf{r})=-\nabla_z\Psi^z-\nabla_{x,y}\varphi(\mathbf{r}). \tag{5}$$

Here, $\varphi(\mathbf{r})$ is the $x-y$ plane potential and we also employ the Bloch theorem for it $\varphi(\mathbf{r})=\varphi_{\mathbf{k}}(\mathbf{r})e^{i\mathbf{k}\cdot\mathbf{r}}$. Then

$$\nabla^2\varphi_{\mathbf{k}}+2i\mathbf{k}\cdot\nabla\varphi_{\mathbf{k}}-\mathbf{k}^2\varphi_{\mathbf{k}}=\nabla\cdot\mathbf{m}_{\mathbf{k}}+i\mathbf{k}\cdot\mathbf{m}_{\mathbf{k}} \tag{6}$$

and $\mathbf{h}_{\mathbf{k}}=-(\nabla\varphi_{\mathbf{k}}+i\mathbf{k}\varphi_{\mathbf{k}})$ is the in-plane (dynamical) component while

$$\nabla^2\Psi^z=\nabla\cdot M_{\mathrm{s}} \tag{7}$$

and $H_{\mathrm{dd}}^z=-\nabla\Psi^z$ is the out-of-plane (static) component. Consequently, the magnon spectra of the antidot lattices can be obtained by solving Eq. (3), Eq. (6), and Eq. (7) self-consistently using the finite element method.

In order to understand the effect of inhomogeneous strain for magnons, we can also map the Eq. (3) into a tight-binding (TB) model with the nearest- and next-nearest-neighbor hopping

$$H=\sum_i t_0(a_i^\dagger a_i+b_i^\dagger b_i)-\sum_{\langle ij\rangle}t_1(a_i^\dagger b_j+\mathrm{H.c.})-\sum_{\langle\langle ij\rangle\rangle}t_2(a_i^\dagger a_j+b_i^\dagger b_j+\mathrm{H.c.}), \tag{8}$$

where $a_i^\dagger$ ($b_i^\dagger$) creates and a_i (b_i) annihilates a magnon on the A (B) sublattice, t_0 is the on-site energy, t_1 is the nearest-neighbor hopping, and t_2 is the next-nearest-neighbor hopping. The energy spectrum is $E_\pm(\mathbf{k})=t_0\pm t_1\sqrt{3+f(\mathbf{k})}-t_2 f(\mathbf{k})$, where $f(\mathbf{k})=2\cos(\sqrt{3}k_x a)+4\cos(\frac{\sqrt{3}}{2}k_x a)\cos(\frac{3}{2}k_y a)$.

In general, inhomogeneous strain effect can strongly modify spectrum in a honeycomb lattice, which is well described by introducing a pseudogauge field $\mathbf{A}(\mathbf{r})$ to the Dirac equation [36–39] (hereafter we take $\hbar=e=1$)

$$H=v_{\mathrm{D}}\begin{pmatrix}\boldsymbol{\sigma}\cdot(\mathbf{q}+\mathbf{A}) & 0\\ 0 & -\boldsymbol{\sigma}^*\cdot(\mathbf{q}-\mathbf{A})\end{pmatrix}. \tag{9}$$

Here, v_{D} is the Dirac velocity, $\boldsymbol{\sigma}=(\sigma_x,\sigma_y)$ are Pauli matrices, and $\mathbf{q}=(q_x,q_y)$ is the momentum measured from the Dirac points in the first Brillouin zone. Therefore, an appropriate spatially varying pseudogauge field $\mathbf{A}(\mathbf{r})$, usually acquired by imposing a specific distortion in an artificial lattice system, can induce a nonzero homogeneous pseudomagnetic field $\mathbf{B}=\nabla\times\mathbf{A}(\mathbf{r})$. Notice that the pseudomagnetic fields felt by magnons at the K and K′ valleys point along opposite directions. Next we will see the pseudomagnetic fields induced by inhomogeneous strain for magnons.

III. RESULTS AND DISCUSSIONS

The magnon band structures of the lowest two bands of triangular antidot lattices obtained from the LLG equation are plotted in Fig. 1(b), using proper parameters for YIG: $\mu_0 H_0=0.5$ T, $M_{\mathrm{s}}=1.94\times10^5$ A/m, and $\lambda_{\mathrm{ex}}=13$ nm [40]. As shown in Fig. 1(b), compared with the case without the DDI (the orange solid lines), we can see that the DDI induces an overall energy shift (the green solid lines) and a minigap at the K (K′) point, about 0.0145 GHz (see the left enlarged inset). As shown in Figs. 1(c) and 1(d), the spatial distributions of $|h_{x,y}|$ at the K (K′) point do not show C_{3v} symmetry; it means that the dynamical components of the DDI break C_{3v} symmetry and open a gap at the K (K′) point. Notice that $|h_{x,y}|$ are quite small compared with $|m_{x,y}|$ and $|H_{\mathrm{dd}}^z|$, and the spatial distributions of $|m_{x,y}|$ show C_{3v} symmetry at the K (K′) point [see Figs. 1(c)–1(g)], therefore the dynamical components of the DDI only induce a minigap at the K (K′) point. In a thick film, the magnon spectrum shows a linear behavior near the Γ point where the dipolar field dominates (the so-called magnetostatic waves) [41]. However, in a thin film (4 nm in this work), the exchange field is very important and cannot be neglected. The magnon spectrum for the lowest-order mode without antidots can be approximately given by [42]

$$\omega=\sqrt{\left(\omega_0+\omega_{\mathrm{M}}\lambda_{\mathrm{ex}}^2k^2\right)\left[\omega_0+\omega_{\mathrm{M}}\lambda_{\mathrm{ex}}^2k^2+\omega_{\mathrm{M}}\left(1-\frac{1-e^{-kt}}{kt}\right)\right]}, \tag{10}$$

where $\omega_0=\gamma(H_0-M_{\mathrm{s}})$, $\omega_{\mathrm{M}}=\gamma M_{\mathrm{s}}$, and t is the thickness of the thin film. When k is near the Γ point, we obtain $\omega\approx\omega_0+\omega_{\mathrm{M}}\lambda_{\mathrm{ex}}^2k^2+\omega_{\mathrm{M}}kt/4$ by performing the Taylor expansion. The magnon spectrum shows a linear behavior only when k is much smaller, due to t being quite small in our work. The magnon spectrum will be dominated by the parabolic behavior quite quickly as k increases due to the strong exchange field. In the presence of the antidot lattices, the effect of the dipolar and exchange field cannot be simply described by Eq. (10) as the solution of $\varphi_{\mathbf{k}}$ depends on the in-plane coordinates, and the magnon dispersion near the Γ point is also no longer linear [as shown in Fig. 1(b)].

Moreover, as shown in Fig. 1(b) by the red solid lines, if we ignore the small dynamical components of the DDI, the energy gap vanishes and the system becomes gapless (see the right enlarged inset). We find that the static component of the DDI is what mainly causes an overall energy shift [Clearly, this feature can also be seen from the Schrödinger equation Eq. (3)]. We find this constant shift is about $\gamma H_{\mathrm{dd}}^z/2\pi=-6.3581$ GHz. Therefore, we will safely neglect the dynamical components and only consider the static component of the DDI in the following discussion for simplicity. As shown in Fig. 1(b) by the red solid lines, one can see that the magnon spectrum displays a Dirac cone at the K (K′) valley of the first Brillouin zone, showing the same behavior

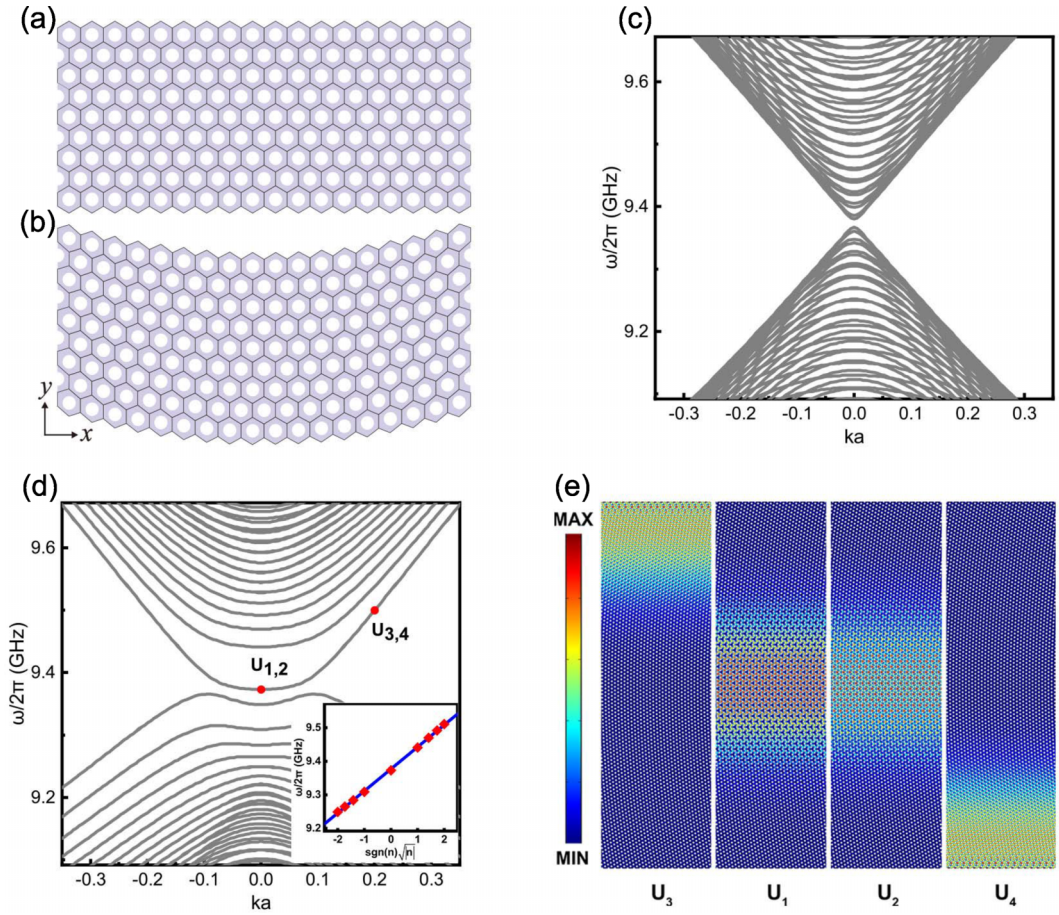

FIG. 2. (a) The illustration of undistorted ribbons of triangular antidot lattices with both the armchair and the zigzag directions. The white dots represent embedded antidots. (b) The illustration of a shear lattice distortion for an armchair-edged ribbon. The magnon band structures of armchair-edged ribbons with a width $L = 8.66$ μm (c) without a shear lattice distortion ($c = 0$) and (d) with a shear lattice distortion ($c = 0.001a^{-1}$) obtained from the LLG equation. The inset of (d) shows the relationship (red solid squares) and the linear fitting (blue solid line) between the magnon Landau levels and Landau indexes at $k = 0$ obtained from the LLG equation. (e) The distributions of the in-plane magnetization $|\mathbf{m}|$ for the three eigenstates labeled in (d), i.e., two bulk ($\mathbf{U_1}$ and $\mathbf{U_2}$) and two edge ($\mathbf{U_3}$ and $\mathbf{U_4}$) states. This distortion corresponds to about 65.4 T for graphene systems.

as electrons in graphene. It means that the magnon inside the patterned YIG thin film can be engineered to the gapless chiral modes.

In addition, a magnonic analog of the TB model can be established and all the hopping constants can be obtained by fitting the magnon band structures at the M and K point obtained by the LLG equation. The fitting hopping parameters are $t_0 = 9.4959$ GHz, $t_1 = 0.681$ GHz, and $t_2 = -0.041$ GHz. As illustrated in Fig. 1(b), when the nearest- and next-nearest neighbor are both taken into consideration, the magnon band structures obtained from the TB model are in good agreement with the numerical results obtained from the LLG equation in a wide frequency range near the Dirac points. In order to study strain effects in triangular antidot lattices, we consider different strain configurations in armchair- and zigzag-edged ribbons with specific inhomogeneous lattice distortions.

For armchair-edged ribbons, a shear lattice distortion with a parabolic distortion vector $u_y = cx^2$, where c denotes the distortion strength, is taken into account, as depicted in Fig. 2(b). Obviously, this type of distortion is symmetric with respect to $x = 0$ and possesses the translation symmetry along the y direction. As shown in Fig. 2(a), the x axis is chosen along a zigzag direction, and the strain-induced pseudovector potential $\mathbf{A}(\mathbf{r})$ is written as $\mathbf{A} = \frac{\beta}{2a}(u_{xx} - u_{yy}, -2u_{xy})$, for a small and smooth distortion [36]. Here β is a dimensionless parameter and $u_{ij} = \frac{1}{2}(\frac{\partial u_i}{\partial x_j} + \frac{\partial u_j}{\partial x_i})$ $(i, j = x, y)$ is the distortion tensor. As a consequence, the linearly varying pseudovector potential is $\mathbf{A} = \beta c(0, -x)/a$ and the homogeneous pseudomagnetic field is $B_z = -\beta c/a$, which is perpendicular to the plane.

The magnon band structures of armchair-edged ribbons obtained from the LLG equation without and with distortions are shown in Figs. 2(c) and 2(d). For undistorted ribbons with $c = 0$ [see Fig. 2(c)], the band structures reveal that the top of the valence band and the bottom of the conduction band is located in $k = 0$ with a direct band gap. This is in analogy with undistorted armchair-edged ribbons of graphene when $N \neq 3M - 1$, where N is the number of dimer lines for armchair-edged ribbons and M is an integer. For distorted ribbons with a smooth distortion $c = 0.001a^{-1}$ [see Fig. 2(d)],

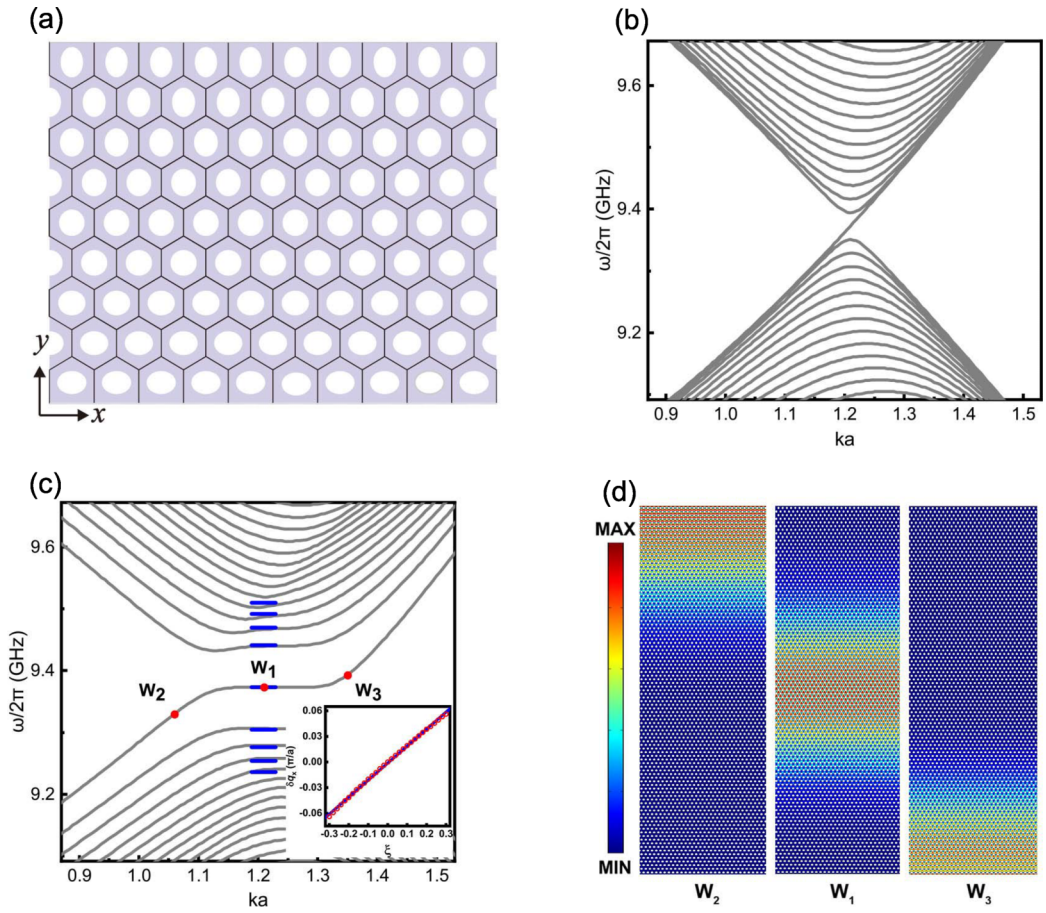

FIG. 3. (a) The illustration of a gradient antidot distortion for a zigzag-edged ribbon. The magnon band structures of zigzag-edged ribbons with a width $L = 7.575$ μm (b) without a gradient antidot distortion ($B_z = 0$) and (c) with a gradient antidot distortion ($B_z = -0.002a^{-2}$) obtained from the LLG equation. The inset of (c) shows that Dirac points shift (red hollow circles) in the momentum space (δq_x), well fitted by a linear dependence (blue solid line) on the shape factor ξ from the LLG eaquation. The blue solid bars represent the analytically predicted magnon Landau levels. (d) The distributions of the in-plane magnetization $|\mathbf{m}|$ for the three eigenstates labeled in (c), i.e., one bulk ($\mathbf{W_1}$) and two edge ($\mathbf{W_2}$ and $\mathbf{W_3}$) states. This distortion corresponds to about 65.4 T for graphene systems.

the magnon bands quantize into a series of the Landau levels of Dirac magnons. The magnon Landau spectrum takes the form

$$\omega_n/2\pi = \omega_0/2\pi + \mathrm{sgn}(n)\omega_c\sqrt{|n|}, \tag{11}$$

where $\omega_c = v_D\sqrt{2|B_z|}$ with $v_D \simeq 3\times10^2$ m/s is a magnonic analog of the cyclotron frequency and n is the Landau index. In Fig. 2(d), the $n = 0$ magnon Landau level separates into two branches owing to the magnonic analog of particle-hole symmetry breaking. Besides, the linear dependence between the Landau level energies and Landau indexes $\sqrt{n}$ at $k = 0$ [see the inset of Fig. 2(d)] indicates the emergence of the magnon Landau levels, from which $\omega_c = 0.0656$ GHz and $\beta \simeq 2$ can be derived in accordance with the slope of the linear relationship.

In order to demonstrate the magnon Landau levels more clearly, we plot the spatial distributions of the lowest magnon Landau level at different momenta and the frequencies of the magnon Landau levels as a function of the indexes n in Fig. 2(e) and the inset of Fig. 2(d), respectively. From Fig. 2(e), one can see that the magnons are localized at the center and edges for zero and finite in-plane momenta, respectively. The linear dependence of the frequencies of the magnon Landau levels on the Landau indexes $\sqrt{n}$ indicates the existence of the magnon Landau levels. The pseudomagnetic fields point along the opposite directions at the K and K′ point, and push magnons towards the opposite edges of the ribbons, leading to magnon valley Hall effect and forming pure magnon valley edge currents $\mathbf{J}_K$ and $\mathbf{J}_{K'}$, as shown in Fig. 1(a).

Next we turn to study the magnon spectra in zigzag-edged ribbons. The pseudomagnetic fields in zigzag-edged ribbons become very different from that in armchair-edged ribbons; if we take an inhomogeneous distortion of the antidot lattices, e.g., $u_y = cy^2$, the distortion would change the shapes of the antidots irregularly as the antidot position varies, especially for large width of ribbon. Recently, a homogeneous pseudomagnetic field was realized in a 2D artificial sonic crystal with a gradient antidot distortion [43]. A similar idea is feasible for magnon zigzag-edged ribbons to create a homogeneous pseudomagnetic field without misshaping honeycomb configuration and changing the size of the unit cell. As displayed in Fig. 3(a), the linearly varying pseudogauge field $\mathbf{A}(\mathbf{r})$ originates from a gradient antidot distortion along the

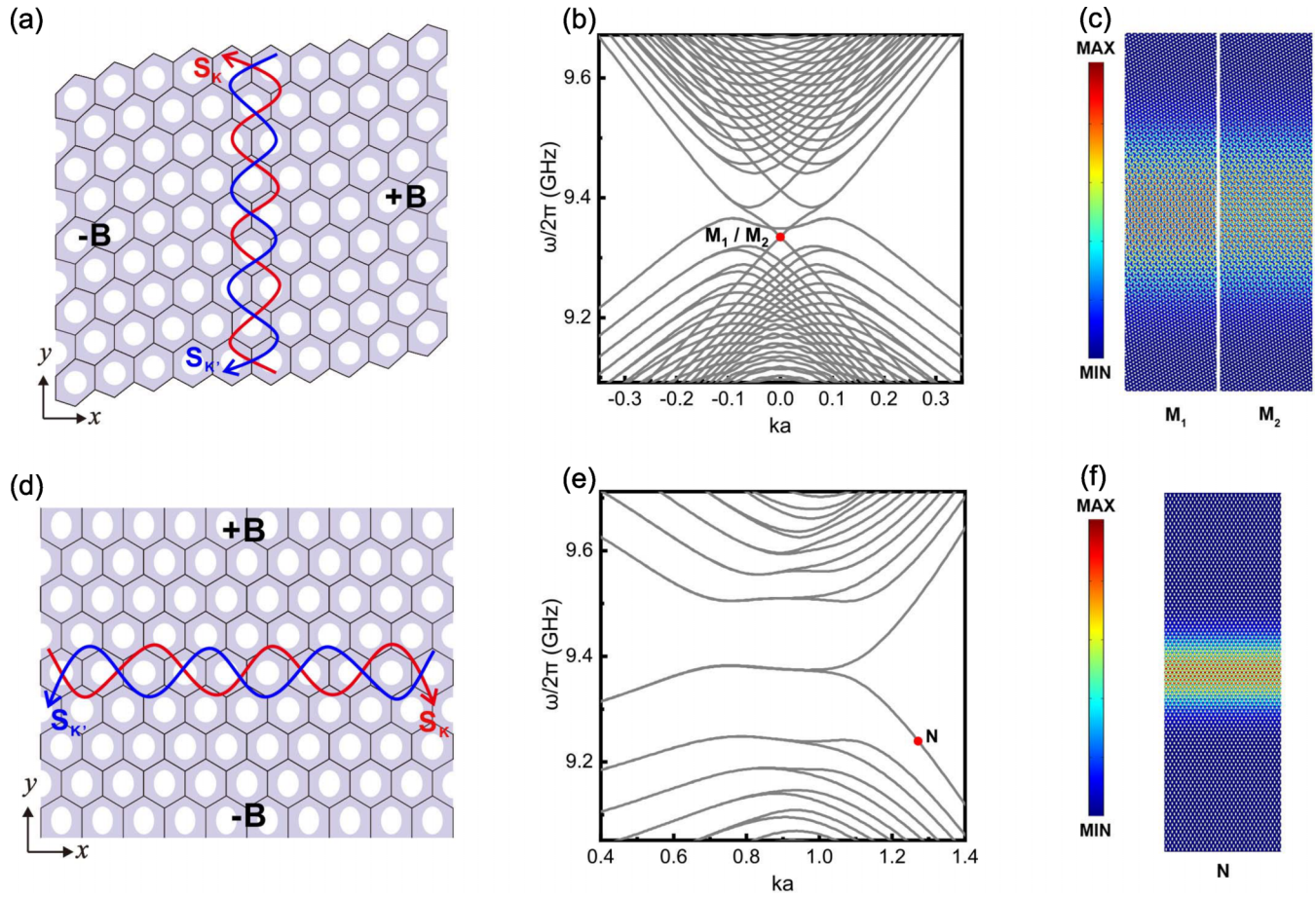

FIG. 4. The illustration of (a) a shear lattice distortion for an armchair-edged ribbon and (d) a gradient antidot distortion for a zigzag-edged ribbon with $\pm\mathbf{B}$ configuration. The pure magnon valley snake orbit currents $\mathbf{S}_K$ and $\mathbf{S}_{K'}$ are serpentine and counterpropagating. The magnon band structures of (b) armchair-edged ribbons with a width $L = 8.66$ μm with an antisymmetric shear lattice distortion ($c = 0.001a^{-1}$) and (e) zigzag-edged ribbons with a width $L = 7.575$ μm with a symmetric gradient antidot distortion ($B_z = -0.01a^{-2}$) obtained from the LLG equation. The distributions of the in-plane magnetization $|\mathbf{m}|$ for the (c) two eigenstates ($\mathbf{M_1}$ and $\mathbf{M_2}$) labeled in (b), and (f) one eigenstate ($\mathbf{N}$) labeled in (e), indicating magnon snake states around the pseudomagnetic field interface.

y direction, while maintaining periodicity in the x direction. When circular-shaped holes are deformed into elliptical-shaped holes, the position shifted $\delta\mathbf{q}$ at the Dirac points occurs along the mirror line in the first Brillouin zone, giving rise to a pseudogauge field $\mathbf{A} = \delta\mathbf{q} = (\delta q_x, 0)$. The shape deviation of an ellipse from a perfect circle will contribute a linearly dependent momentum shift, which is characterized by a simple formula $\delta q_x = c_\gamma \xi$. Here $\xi = (q - p)/p$ is a dimensionless shape factor with p and q being semimajor and semiminor axis of elliptical-shaped holes and c_γ is a coefficient associated with an area ratio $\gamma = 2\pi pq/3\sqrt{3}a^2$ of ellipses to hexagons. As a result, a homogeneous pseudomagnetic field $B_z = -A_x(y)/y$ can be achieved by adopting a linearly varying shape factor $\xi(y) = -B_z y/c_\gamma$ of antidots along the y direction.

The inset of Fig. 3(c) shows the momentum shift of the Dirac points linearly varying with the shape factor obtained from the LLG equation with $c_\gamma = 0.1993\pi/a$ at $\gamma \simeq 0.3$. The magnon band structures of zigzag-edged ribbons without and with distortions from the LLG equation are shown in Figs. 3(b) and 3(c). For undistorted ribbons with the pseudomagnetic field $B_z = 0$ [see Fig. 3(b)], similar to undistorted zigzag-edged ribbons of graphene, the top of the valence band and the bottom of the conduction are degenerate at $|k|a = 2\pi/3\sqrt{3}$. For distorted ribbons with the pseudomagnetic field $B_z = -0.002a^{-2}$ [see Fig. 3(c)], the flat and discrete magnon Landau levels clearly appear in the vicinity of the Dirac frequency and its energies obtained numerically agree very well with the analytical results [see the blue solid bars in Fig. 3(c)]. For instance, the first Landau level gap Δ_1 is 0.066 GHz in numerical results, which virtually agrees with $\Delta_1 = 0.065$ GHz in analytical results obtained from Eq. (11).

In order to depict the mangon Landau levels, which are caused by inhomogeneous distortions, more clearly in zigzag case, we draw the spatial distributions of the in-plane magnetization $|\mathbf{m}|$ in Fig. 3(d). The spatial distributions of the lowest magnon Landau level at $ka = 2\pi/3\sqrt{3}$ is localized at the center of the zigzag-edged ribbon. While for the finite momenta near the K and K′ valleys, magnons accumulate at the opposite edges of the zigzag-edged ribbon [see Fig. 3(d)], leading to magnon valley Hall effect and forming pure magnon valley edge currents $\mathbf{J}_K$ and $\mathbf{J}_{K'}$, as shown in Fig. 1(a).

Compared with the real magnetic lattices, artificial antidot lattices can be used to design various and arbitrary distortions and pseudomagnetic fields by manipulating antidot arrays. In the previous discussions, we only study one case where inhomogeneous distortions can induce homogeneous pseudomagnetic fields. It is interesting to consider another simple case where the inhomogeneous distortions induce inhomogeneous pseudomagnetic fields, e.g., $\pm\mathbf{B}$ configuration. In this case, the pseudomagnetic field is reversed on both sides of the ribbon, constructing a pseudomagnetic field interface or domain wall at the center of the ribbon. For armchair-edged ribbons, schematically shown in Fig. 4(a), the shear lattice distortion is antisymmetric with the distortion vector given by $u_y = \mathrm{sgn}(x)cx^2$ and the corresponding pseudomagnetic field is $B_z = -\mathrm{sgn}(x)\beta c/a$. For zigzag-edged ribbons, schematically shown in Fig. 4(d), the gradient antidot distortion and the linearly varying pseudogauge field $\mathbf{A}(\mathbf{r})$ are both symmetric with respect to $y = 0$, generating two equal but oppositely directed pseudomagnetic fields, $B_z = -\mathrm{sgn}(y)A_x(y)/y$.

We show the magnon band structures for studied armchair- and zigzag-edged ribbons under this inhomogeneous pseudomagnetic field in Figs. 4(b) and 4(e), respectively. The $\pm\mathbf{B}$ configuration of the pseudomagnetic fields lifts degeneracies of the band and induces the band splitting. In contrast to the homogeneous pseudomagnetic fields, the oppositely directed pseudomagnetic fields on the two sides of the ribbon result in the extraordinary states, known as magnon snake states. These states are described by Figs. 4(c) and 4(f), which display the spatial distributions of the in-plane magnetization $|\mathbf{m}|$ of the splitting states. Apparently, these magnon snake states are spatially located at the center of the ribbon. Therefore, if a microwave driving field is applied to the antidot lattices to excite spin waves, one shall be able to observe a serpentine manner of snake states due to the cyclotron motion originating from the pseudomagnetic field $\pm\mathbf{B}$, schematically shown in Figs. 4(a) and 4(d), respectively. Thus, the counterpropagating pure magnon valley snake orbit currents $\mathbf{S}_{\mathrm{K}}$ and $\mathbf{S}_{\mathrm{K}'}$ are formed.

IV. CONCLUSIONS

In summary, we propose the pure magnon valley currents in a patterned FTF. By engineering the artificial antidot lattices, we can generate a homogeneous pseudomagnetic field up to 60 T for magnons, which pushes magnons at the K and K′ valleys towards the opposite edges of FTFs, leading to magnon valley Hall effect and forming pure magnon valley edge currents. We also propose that an inhomogeneous pseudomagnetic field induces magnon snake states at the center of the ribbon and form pure magnon valley snake orbit currents. These robust edge states and snake states offer us new dissipationless channels for spin transport, and a new way to construct new spintronic devices.

ACKNOWLEDGMENTS

This work is supported by MOST of China (Grant No. 2018YFA0306101), the National Natural Science Foundation of China (NSFC) (Grants No. 11974340 and No. 92265203), the Chinese Academy of Sciences (Grants No. XDB28000000, No. QYZDJ-SSW-SYS001, and No. XDPB22).

[1] A. V. Chumak, V. Vasyuchka, A. Serga, and B. Hillebrands, Magnon spintronics, Nat. Phys. **11**, 453 (2015).
[2] V. V. Kruglyak, S. O. Demokritov, and D. Grundler, Magnonics, J. Phys. D **43**, 264001 (2010).
[3] A. A. Serga, A. V. Chumak, and B. Hillebrands, YIG magnonics, J. Phys. D **43**, 264002 (2010).
[4] A. Hoffmann and S. D. Bader, Opportunities at the Frontiers of Spintronics, Phys. Rev. Appl. **4**, 047001 (2015).
[5] V. Cherepanov, I. Kolokolov, and V. L'vov, The saga of YIG: spectra, thermodynamics, interaction and relaxation of magnons in a complex magnet, Phys. Rep. **229**, 81 (1993).
[6] Y. Sun, Y.-Y. Song, H. Chang, M. Kabatek, M. Jantz, W. Schneider, M. Wu, H. Schultheiss, and A. Hoffmann, Growth and ferromagnetic resonance properties of nanometer-thick yttrium iron garnet films, Appl. Phys. Lett. **101**, 152405 (2012).
[7] J. Barker and G. E. W. Bauer, Thermal Spin Dynamics of Yttrium Iron Garnet, Phys. Rev. Lett. **117**, 217201 (2016).
[8] T. Liu and G. Vignale, Electric Control of Spin Currents and Spin-Wave Logic, Phys. Rev. Lett. **106**, 247203 (2011).
[9] A. Kamra, H. Keshtgar, P. Yan, and G. E. W. Bauer, Coherent elastic excitation of spin waves, Phys. Rev. B **91**, 104409 (2015).
[10] P. Gruszecki, Y. S. Dadoenkova, N. N. Dadoenkova, I. L. Lyubchanskii, J. Romero-Vivas, K. Y. Guslienko, and M. Krawczyk, Influence of magnetic surface anisotropy on spin wave reflection from the edge of ferromagnetic film, Phys. Rev. B **92**, 054427 (2015).
[11] W. Yu, J. Lan, R. Wu, and J. Xiao, Magnetic Snell's law and spin-wave fiber with Dzyaloshinskii-Moriya interaction, Phys. Rev. B **94**, 140410(R) (2016).
[12] Y. Jiang, H. Y. Yuan, Z.-X. Li, Z. Wang, H. W. Zhang, Y. Cao, and P. Yan, Twisted Magnon as a Magnetic Tweezer, Phys. Rev. Lett. **124**, 217204 (2020).
[13] J. Fransson, A. M. Black-Schaffer, and A. V. Balatsky, Magnon Dirac materials, Phys. Rev. B **94**, 075401 (2016).
[14] S. S. Pershoguba, S. Banerjee, J. C. Lashley, J. Park, H. Ågren, G. Aeppli, and A. V. Balatsky, Dirac magnons in honeycomb ferromagnets, Phys. Rev. X **8**, 011010 (2018).
[15] B. Yuan, I. Khait, G.-J. Shu, F. C. Chou, M. B. Stone, J. P. Clancy, A. Paramekanti, and Y.-J. Kim, Dirac magnons in a honeycomb lattice quantum XY magnet $CoTiO_3$, Phys. Rev. X **10**, 011062 (2020).
[16] Y.-M. Li, J. Xiao, and K. Chang, Topological magnon modes in patterned ferrimagnetic insulator thin films, Nano Lett. **18**, 3032 (2018).
[17] M. Gibertini, A. Singha, V. Pellegrini, M. Polini, G. Vignale, A. Pinczuk, L. N. Pfeiffer, and K. W. West, Engineering artificial graphene in a two-dimensional electron gas, Phys. Rev. B **79**, 241406(R) (2009).

[18] S. Li, W.-X. Qiu, and J.-H. Gao, Designing artificial two dimensional electron lattice on metal surface: a Kagome-like lattice as an example, Nanoscale **8**, 12747 (2016).

[19] M. C. Rechtsman, J. M. Zeuner, A. Tünnermann, S. Nolte, M. Segev, and A. Szameit, Strain-induced pseudomagnetic field and photonic Landau levels in dielectric structures, Nat. Photon. **7**, 153 (2013).

[20] C. Brendel, V. Peano, O. J. Painter, and F. Marquardt, Pseudomagnetic fields for sound at the nanoscale, Proc. Natl. Acad. Sci. USA **114**, 3390 (2017).

[21] Y.-M. Li, X. Zhou, Y.-Y. Zhang, D. Zhang, and K. Chang, Dirac fermions and pseudomagnetic fields in two-dimensional electron gases with triangular antidot lattices, Phys. Rev. B **96**, 035406 (2017).

[22] H. Abbaszadeh, A. Souslov, J. Paulose, H. Schomerus, and V. Vitelli, Sonic Landau Levels and Synthetic Gauge Fields in Mechanical Metamaterials, Phys. Rev. Lett. **119**, 195502 (2017).

[23] Y. Ferreiros and M. A. H. Vozmediano, Elastic gauge fields and Hall viscosity of Dirac magnons, Phys. Rev. B **97**, 054404 (2018).

[24] O. Jamadi, E. ZRozas, G. Salerno, M. Milićević, T. Ozawa, I. Sagnes, A. Lemaître, L. Le Gratiet, A. Harouri, I. Carusotto, J. Bloch, and A. Amo, Direct observation of photonic Landau levels and helical edge states in strained honeycomb lattices, Light Sci. Appl. **9**, 144 (2020).

[25] H. Yu, O. d'Allivy Kelly, V. Cros, R. Bernard, P. Bortolotti, A. Anane, F. Brandl, F. Heimbach, and D. Grundler, Approaching soft X-ray wavelengths in nanomagnet-based microwave technology, Nat. Commun. **7**, 11255 (2016).

[26] S. Maendl, I. Stasinopoulos, and D. Grundler, Spin waves with large decay length and few 100 nm wavelengths in thin yttrium iron garnet grown at the wafer scale, Appl. Phys. Lett. **111**, 012403 (2017).

[27] C. Liu, J. Chen, T. Liu, F. Heimbach, H. Yu, Y. Xiao, J. Hu, M. Liu, H. Chang, T. Stueckler, S. Tu, Y. Zhang, Y. Zhang, P. Gao, Z. Liao, D. Yu, K. Xia, N. Lei, W. Zhao, and M. Wu, Long-distance propagation of short-wavelength spin waves, Nat. Commun. **9**, 738 (2018).

[28] K. Baumgaertl, J. Gräfe, P. Che, A. Mucchietto, J. Förster, N. Träger, M. Bechtel, M. Weigand, G. Schütz, and D. Grundler, Long-distance propagation of short-wavelength spin waves, Nano Lett. **20**, 7281 (2020).

[29] P. Wang, H. Zhao, S. Liu, Y. Y. Chin, H. J. Lin, B. M. Zhang, Z. Yuan, S. W. Jiang, H. F. Ding, J. Du, Q. Y. Xu, K. Xia, and D. Wu, Reduced interfacial magnetic moment of $Y_3Fe_5O_{12}$ by capping Pt, Appl. Phys. Lett. **113**, 182402 (2018).

[30] H. Wang, J. Chen, T. Liu, J. Zhang, K. Baumgaertl, C. Guo, Y. Li, C. Liu, P. Che, S. Tu, S. Liu, P. Gao, X. Han, D. Yu, M. Wu, D. Grundler, and H. Yu, Chiral Spin-Wave Velocities Induced by All-Garnet Interfacial Dzyaloshinskii-Moriya Interaction in Ultrathin Yttrium Iron Garnet Films, Phys. Rev. Lett. **124**, 027203 (2020).

[31] J. Ding, C. Liu, Y. Zhang, U. Erugu, Z. Quan, R. Yu, E. McCollum, S. Mo, S. Yang, H. Ding, X. Xu, J. Tang, X. Yang, and M. Wu, Nanometer-Thick Yttrium Iron Garnet Films with Perpendicular Anisotropy and Low Damping, Phys. Rev. Appl. **14**, 014017 (2020).

[32] M. G. Cottam, in *Linear and Nonlinear Spin Waves in Magnetic Films and Superlattices* (World Scientific, Singapore, 1994), p. 4.

[33] H. Yu, O. d'Allivy Kelly, V. Cros, R. Bernard, P. Bortolotti, A. Anane, F. Brandl, R. Huber, I. Stasinopoulos, and D. Grundler, Magnetic thin-film insulator with ultra-low spin wave damping for coherent nanomagnonics, Sci. Rep. **4**, 6848 (2014).

[34] G. Rado and J. Weertman, Spin-wave resonance in a ferromagnetic metal, J. Phys. Chem. Solids **11**, 315 (1959).

[35] Y. Haiming, X. Jiang, and S. Helmut, Magnetic texture based magnonics, Phys. Rep. **905**, 176802 (2021).

[36] A. H. Castro Neto, F. Guinea, N. M. R. Peres, K. S. Novoselov, and A. K. Geim, The electronic properties of graphene, Rev. Mod. Phys. **81**, 109 (2009).

[37] Z. Wu, F. Zhai, F. M. Peeters, H. Q. Xu, and K. Chang, Valley-Dependent Brewster Angles and Goos-H Anchen Effect in Strained Graphene, Phys. Rev. Lett. **106**, 176802 (2011).

[38] Y. Jiang, T. Low, K. Chang, M. I. Katsnelson, and F. Guinea, Generation of Pure Bulk Valley Current in Graphene, Phys. Rev. Lett. **110**, 046601 (2013).

[39] D.-B. Zhang, G. Seifert, and K. Chang, Strain-Induced Pseudomagnetic Fields in Twisted Graphene Nanoribbons, Phys. Rev. Lett. **112**, 096805 (2014).

[40] M. Krawczyk and H. Puszkarski, Magnonic excitations versus three-dimensional structural periodicity in magnetic composites, Cryst. Res. Technol. **41**, 547 (2006).

[41] D. D. Stancil and A. Prabhakar, in *Spin Waves: Theory and Applications* (Springer, Berlin, 2009), p. 155.

[42] B. Kalinikos, Excitation of propagating spin waves in ferromagnetic films, IEE Proc. H **127**, 4 (1980).

[43] X. Wen, C. Qiu, Y. Qi, L. Ye, M. Ke, F. Zhang, and Z. Liu, Acoustic Landau quantization and quantum-Hall-like edge states, Nat. Phys. **15**, 352 (2019).